

Orientation-Driven Chirality Funnels in Chiral Low-Dimensional Lead-Halide Perovskite Heterostructures

Shangpu Liu,^{1,2,3*} Jonathan Zerhoch,^{1,2} Markus W. Heindl,^{1,2} Chaoran Zhang,^{1,4,5} Tim Kodalle,⁶ Kun Sun,⁷ Andrii Shcherbakov,^{1,2} Stanislav Bodnar,¹ Milon Miah,¹ Mohammad Gholipoor,³ Christian Jandl,^{5,8} Alexander Pöthig,^{5,8} Joachim Ballmann,⁹ Ian D. Sharp,² Peter Müller-Buschbaum,⁷ Carolin M. Sutter-Fella,⁶ Ulrich W. Paetzold,³ Felix Deschler^{1*}

¹Physikalisch-Chemisches Institut, Universität Heidelberg,
Im Neuenheimer Feld 229, 69120 Heidelberg, Germany

²Walter Schottky Institute and Department of Physics, TUM School of Natural Sciences,
Technical University of Munich, Am Coulombwall 4, 85748 Garching, Germany

³Institute of Microstructure Technology, Karlsruhe Institute of Technology, 76344 Eggenstein-Leopoldshafen, Germany; Light Technology Institute, Karlsruhe Institute of Technology, 76131 Karlsruhe, Germany,

⁴Department of Chemistry, National University of Singapore,
3 Science Drive 3, 117543, Singapore

⁵Chemistry Department, TUM School of Natural Sciences, Technical University of Munich,
Lichtenbergstraße 4, 85748 Garching, Germany

⁶Molecular Foundry, Lawrence Berkeley National Laboratory, 1 Cyclotron Rd., Berkeley, CA
94720, USA

⁷Chair for Functional Materials, Department of Physics, TUM School of Natural Sciences,
Technical University of Munich, James-Franck-Straße 1, 85748 Garching, Germany

⁸Catalysis Research Center, Technical University of Munich, Ernst-Otto-Fischer-Straße 1, 85748 Garching, Germany

⁹Anorganisch-Chemisches Institut, Universität Heidelberg, Im Neuenheimer Feld 276, 69120 Heidelberg, Germany

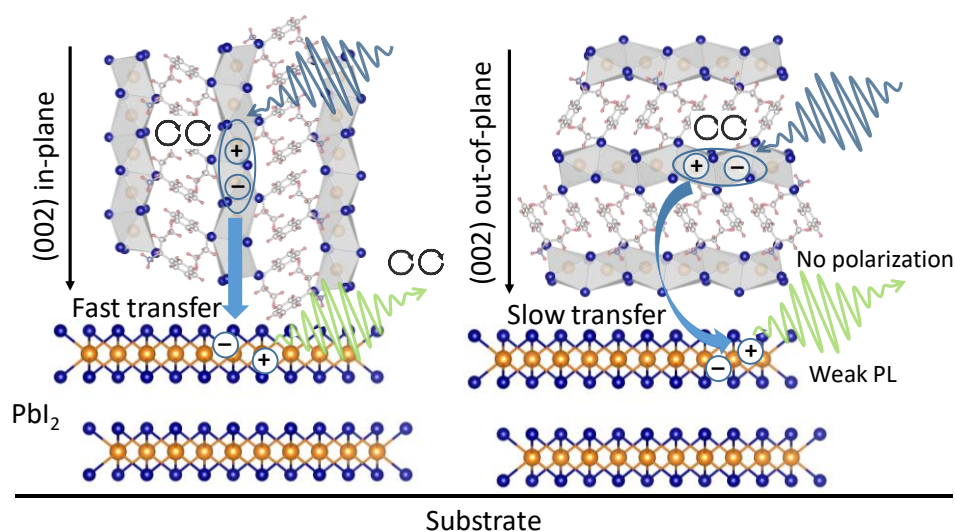
*Correspondence and requests for materials should be addressed to

F. D. (email: deschler@uni-heidelberg.de); S.L. (email: shangpu.liu@kit.edu)

Abstract

Chiral hybrid metal-halide perovskites show low-symmetry crystal structures, large Rashba splitting, spin-filtering, and strong chiroptical activity. Circular dichroism and circularly polarized photoluminescence have been investigated in chiral perovskites with increasingly distorted chiral structures. Here, we report the fabrication of chiral (R/S)-EAPbI₃ (EA = α -ethylbenzylamin) single crystals, which possess highly distorted octahedral structures with a high angle variance value of $\sim 68^\circ$. Using control in the fabrication conditions, we transfer chiral single crystals to thin films and achieve different crystal orientation preferences that induce tuneable chiroptical properties to their heterostructures with PbI₂ nanodomains, which we characterize with in-situ X-ray diffraction and grazing-incidence wide-angle X-ray scattering measurements. Using transient chiroptical spectroscopies, we resolve photoexcited charge carrier dynamics and chirality transfer processes in such heterostructures down to cryogenic temperatures. We observe rapid carrier transfer along the in-plane (002) facets in chiral perovskite phases to PbI₂ nanostructures within the initial few picoseconds, while carrier transfer along the out-of-plane (002) facets occurs at a slower rate. This fast transfer process leads to high photoluminescence intensities and large degrees of circular polarization in the emission from PbI₂ nanodomains. Our findings report a multi-dimensional chiral-achiral heterostructures which takes advantage of controllable chirality transfer and offer new routes for future spintronic and chiroptical applications.

TOC



Introduction

Hybrid metal-halide perovskites have shown great potential for future optoelectronic devices, including light-emitting diodes^{1,2}, photodetectors^{3,4}, solar cells⁵, and lasers⁶, due to their excellent emission quantum efficiencies, promising charge-transport properties, and strong defect tolerance. By changing the organic components and inorganic elements, hybrid perovskite materials offer diverse opportunities for tailoring crystal structures, band edge electronic structures, and resulting optical properties. Indeed, owing to their tuneable composition, variable bandgaps, and strong spin-orbit coupling, hybrid perovskites are of particular interest for multifunctional applications, such as for polarized light generation and detection⁷⁻⁹, second harmonic generation¹⁰, piezoelectrics^{11,12}, and spintronics^{13,14}. It has been reported that, by embedding chiral organic molecules into hybrid perovskites, distorted low-symmetry perovskite crystal structures can be achieved. The resulting chiral perovskites belong to Sohncke space groups^{15,16}. These materials frequently exhibit promising chiroptical features due to their chiral crystal structures and broken inversion symmetry^{15,17}.

Two main routes can be exploited for the formation of chiral perovskites. One route is to use chiral organic molecules as ligands to create chiral perovskite nanocrystals¹⁸⁻²⁰, which tend to exhibit high PL intensities due to quantum confinement, but relatively low degrees of chiroptical polarization and limited stability. Another route is using chiral organic cations within the material itself to form chiral perovskite crystal structures¹⁵⁻¹⁷. However, the introduction of chirality into perovskite structures leads to the formation of low-dimensional perovskites because of the large chiral organic groups that are required, which decrease their conductivity and often also photoluminescence quantum efficiency (PLQE) due to increased trap state concentrations and strong electron-phonon coupling^{9,21}. Recently, low-dimensional chiral hybrid perovskites with high PLQE at room temperature have been reported⁹. Notably, chiral two-dimensional (2D) layered perovskites are well-known for their high degree of circularly polarized photoluminescence (CPL) polarization in their single crystal or exfoliated forms^{7,9,12}. However, the degree of CPL polarization for thin film samples remains in the low percentage range^{22,23}. Additionally, most reported work about chiral one-dimensional (1D) chain perovskites focuses on their strong circular dichroism (CD) signals, which can be utilized for circularly polarized light detection^{3,4}. However, due to their disconnected face-sharing octahedral chains, chiral 1D perovskites show weak PL intensities at

room temperature, and only very low CPL was reported from chiral 1D perovskites, which prevents their use for optoelectronic applications.

Chiral 1D perovskites can differentially absorb circularly polarized light, but not efficiently emit light^{17,24}. Here, we report a simple solution-processed method for fabricating chiral perovskite/PbI₂ heterostructure thin films wherein the chiral properties of chiral perovskite are effectively transferred to PbI₂ nanostructures. The resulting heterostructures exhibit broad CD signals, covering the spectral range of 300 nm - 550 nm, and a large degree of CPL polarization at low temperatures (~4%), which is comparable to chiral 2D perovskite thin films^{15,16,22,23}. In addition, we show that solvent engineering promotes chiral perovskite/PbI₂ heterostructure formation. Using single crystal X-ray diffraction (SCXRD) of bulk materials, in-situ XRD during subsequent film synthesis, and grazing incident wide-angle X-ray scattering (GIWAXS) of the fabricated films, we analyze in-situ spin-coated thin films and relate fast carrier funnels to preferential crystal orientations within chiral perovskite/PbI₂ thin films. We further investigate the carrier and chirality transfer dynamics in chiral perovskite heterostructures by transient chiroptical spectroscopy and rationalize the enhanced angular momentum polarization lifetime and CPL to arise from fast and effective carrier transfer from the chiral perovskite phase to PbI₂ heterostructures. Our findings indicate the potential of solution-processed chiral perovskite heterostructure thin films for future optoelectronic and spintronic applications.

Results and Discussion

Structural and emission characteristics of chiral 1D perovskite crystals

We prepared chiral 1D perovskite (R/S/Rac)-EAPbI₃ single crystals by slow cooling. In brief, after fully dissolving (R/S/Rac)-EA and PbO in HI solution at 95 °C, we controllably cooled the reaction vessel down to room temperature at a rate of ~ 1 °C/h. During cooling, large needle-shaped single crystals formed gradually (Fig. S1). SCXRD measurements were used to identify the crystal structures of the resulting chiral perovskites (see detailed crystal structure results in Table S1), which comprise 1D chains of distorted face-sharing PbI₃ octahedra surrounded by alternating chiral organic molecules (Fig. 1a and 1b). Chiral (R) and (S) 1D perovskite samples have a similar mirror-like crystal structure, both crystallizing in an orthorhombic $P 2_12_12_1$ space group, which

belongs to one of the Sohncke space groups¹⁵ and confirming successful chirality transfer from chiral organics to the inorganic lead halide chains.

SCXRD analysis reveals a prominent structure distortion in our chiral 1D perovskites. Both chiral (R) and (S) single crystals show varied Pb-I bond distances from 3.08 to 3.43 Å, with a similar octahedral bond length distortion index of 0.027 (Detailed calculations in [Table S2](#)), which should be zero for a perfect octahedron with full symmetry. Importantly, a much higher angle variance value of ~68 is observed for our chiral 1D perovskites, which is among the highest values among the so far reported chiral perovskite semiconductors²⁵, indicating the strongly broken symmetry in our chiral 1D perovskites. Besides, we find chiral 1D perovskite (R), (S), and (Rac)-EAPbI₃ crystals all exhibit broad-band emissions at sub-band positions (400 – 750 nm, [Fig. 1c](#)). We attribute such broad-band emission to the trapped excitons, which have been widely reported in low dimensional perovskites^{26–28}. There is no obvious free exciton PL signal observed in our chiral 1D perovskite single crystals, similar to other 1D perovskites^{4,24}, which may hinder their chiroptical applications. However, we hypothesize that the strong chirality present in our chiral 1D perovskite crystal structures, which can be also used for efficient polarized carrier injections, beyond the limit of pure phase chiral materials.

Fabrication of chiral perovskite/PbI₂ heterostructures

For compatibility with optoelectronic applications, we next converted single-crystal samples to polycrystalline thin films using a simple solution-based spin-coating method (see details in [Materials and Methods](#) section). Thin film fabrication yields heterostructures of chiral 1D perovskites and PbI₂ nanodomains, as we will show in the following. We used three different solvents (DMF, DMSO, and a mixture of DMSO and DMF in equal volumes) to dissolve perovskite single crystals and studied how the solvents impact the film structure and morphology. The obtained precursor solutions were directly spin-coated on glass substrates that were pre-cleaned with oxygen plasma. The corresponding samples are henceforth denoted as DMF, DMSO, and DMSO-DMF films. The same solvent engineering methods were used to control the CPL of chiral 2D perovskite/QDs compositions²⁹.

To directly monitor the crystallization of the perovskite films, we performed in-situ XRD measurements. As depicted in Fig. 2a and 2b, as well as the extended range in-situ XRD results shown in Fig. S2, no obvious diffraction signal is observed within the initial 60 s, which includes the complete spin-coating process. However, once thermal annealing (100 °C) was initiated at 60 s, a transient intermediate state, characterized by a diffraction peak at 7.3°, emerged, which subsequently gradually diminished and vanished after ~300 s for DMF and DMSO-DMF films, but more quickly (~100 s) for the pure DMSO film. Importantly, the (002) reflection from the chiral 1D perovskites, located at 8.2°, appeared at ~100 s and then remained stable through the end of the experiment. Much stronger (002) diffraction intensities were observed in the DMF films compared to the other two films, as discussed below. In addition, a reflection located at 14.3° appeared after 100 s for DMSO-DMF film, while this signal was weaker for the DMSO film, and much weaker for the pure DMF film. Compared to simulated patterns derived from the both chiral perovskite and PbI₂ single crystal structures (Fig. S3), we attribute this new reflection pattern to the (001) facet of PbI₂. In summary, the chiral 1D perovskite films show similar characteristics, though with a dominant (002) reflection due to the thin film texture, while stronger PbI₂ signals were observed in DMSO-DMF samples, indicating the formation of chiral perovskite/PbI₂ heterostructures. We note that there is a rather broad background signal at higher angles for the DMSO and DMSO-DMF samples that is not present for the DMF sample. This may relate to the presence of an amorphous or highly disordered phase.

To further investigate the crystal orientations within chiral perovskite films, we performed GIWAXS measurements using synchrotron radiation. For the spin-coated perovskite films without subsequent thermal annealing (Fig. 2c), smooth diffraction rings are observed, indicating highly randomized distributions of the crystal orientations within the polycrystalline perovskite films. However, for the perovskite films that were thermally annealed at 100 °C for 10 min after spin coating (Fig. 2d and S4), we observe several intense Bragg spots within each ring, which indicates preferential crystal orientations in the films. Out-of-plane PbI₂ (001) reflection appears in all three films after annealing process (Fig. S4). Besides, the dominant (002) reflection in chiral perovskite phases corresponds to the preferred out-of-plane orientation for all three types of films. However, for DMSO-DMF and DMSO films, we observe an additional in-plane (002) contribution. Thus, the mixed orientations within these films may explain the weaker (002) reflection intensities

observed during in-situ XRD measurements (Fig. 2a). Alongside the (002) reflection, an in-plane (011) contribution is observed for the DMF films. For DMSO-DMF films, the detection of smooth diffraction rings indicates a random orientation of (011) planes.

Overall, our GIWAXS measurements indicate that the solvents used during the spin-coating process influence the crystal orientations within the perovskite films, similar to recent reported work³⁰, which uses Cl substitutes to vary film growth orientations. The (002) orientation along the out-of-plane direction is dominant in DMF films, while DMSO-DMF and DMSO films contain some material with in-plane or random (002) / (011) orientations. Similar trends are also found in atomic force microscope (AFM) measurements, in which different solvents lead to different surface morphologies, which may also relate to their thin film textures (Fig. S5).

General optical characteristics of chiral perovskite/PbI₂ films

Considering the interesting chiral structures of these 1D perovskite films and their solvent-tuneable morphologies, we now study their optical properties. Steady-state absorption spectra show that our chiral perovskite films exhibit an excitonic absorption peak at ~378 nm for all three solvents (Fig. 3a), which indicates a band gap that is similar to the reported 1D perovskites^{4,24,27}. Fig. 3b presents the circular dichroism (CD) results from the chiral 1D (R)-EAPbI₃ perovskite films. Importantly, the main CD signals from chiral perovskite films are located at the absorption band positions (~378 nm), demonstrating chirality transfer from the chiral organic molecules to the metal-halide moieties. The same result is also obtained from analysis of the absorption anisotropy factors (g_{abs}) (see detailed calculations in Fig. S6a), which are independent of film thickness and absorption intensities^{15,31,32}. Opposite CD signals are observed for (R/S)-EAPbI₃ films, while no CD signals are found in racemic-EAPbI₃ films (Fig. S6b). Importantly, we find that different solvents resulted in pronounced changes to the CD signals. Perovskite films formed from DMF solvents show the largest CD signal, which we relate to variations in their film texture (Fig. 2).

Next, we study the PL of our chiral 1D perovskite films. Under 340 nm excitation, no PL signal is observed at the band edge (~378 nm) for any of the films, regardless of the solvent used for their preparation (Fig. S7). This observation is reasonable, considering that most reported chiral 1D perovskites do not exhibit band edge PL due to indirect band structures^{4,24}. Notably, a weak sub-

gap PL band appears at ~ 510 nm in our chiral perovskite films (Fig. 3c), along with a broad PL feature located from 550 nm to 650 nm that we attribute to a trapped exciton, consistent with what we find before from single crystals (Fig. 1c)²¹. Using different solvents changes the intensity of this trapped-exciton PL signal, with the highest intensities in DMF films and lowest intensities in DMSO-DMF films. However, the origin of the PL peak at 510 nm is less clear. To identify this feature, we prepare pure PbI₂ thin films using identical spin-coating conditions (40 mg PbI₂ dissolved in 200 μ L DMSO-DMF solutions), which show a yellowish color compared to transparent chiral 1D perovskite films (Fig. S8). The pure PbI₂ films show a PL feature at ~ 510 nm (Fig. 3c), which has been widely reported before^{33,34}. We further compared the absorption spectra between pure PbI₂, (R)-EAPbI₃, and (R)-EAPbI₃ films with excess PbI₂ added into the spin-coating solution. We find that both PbI₂ and (R)-EAPbI₃ films with excess PbI₂ show a noticeable absorption band feature at 500 nm, which overlaps well with the shoulder in the absorption signals of pristine (R)-EAPbI₃ films (Fig. 3a and Fig. S9a). In addition, XRD and GIWAXS measurements indicate the presence of PbI₂ phases in chiral perovskite films (Fig. 2, Fig. S4 and Fig. S9b). Thus, we conclude that the 500 nm feature in (S/R)-EAPbI₃ films originate from a chiral perovskite/PbI₂ heterostructure comprising low-dimensional PbI₂ nanodomains³⁵. Besides, we also add additional (R)-EAI precursor in spin-coating solutions to prepare (R)-EAPbI₃ films, such 500 nm absorption shoulder disappears, which is another clear evidence due to the consumption of all PbI₂ in the films (Fig. S10).

To study the mechanism behind the formation of the ~ 510 nm PL feature from the PbI₂ nanodomains, we performed transient absorption (TA) spectroscopy measurements on our chiral 1D perovskite/PbI₂ heterostructures (Fig. 3d-f). Two ground-state bleach (GSB) signals were observed from TA spectroscopy. One feature (GSB1), located at ~ 378 nm, originates from the 1D perovskite band edge, while a second bleach signal (GSB2) at ~ 495 nm corresponds to the ~ 510 nm PL feature with a Stokes shift of ~ 15 nm³⁶. For reference, we also prepared one chiral perovskite sample using DMF as a solvent but without subsequent thermal annealing. The corresponding TA spectrum from this reference sample reveals that no GSB2 feature is present, suggesting that the associated perovskite/PbI₂ heterostructure is not formed in the absence of annealing (Fig. 3g). In contrast, the GSB2 feature is present for pure PbI₂ films and all studied chiral 1D perovskite/PbI₂ heterostructures and following the 10 min thermal annealing process

(Fig. S11). However, the solvent strongly influences this signal's magnitude, with both DMSO-DMF and DMSO films exhibiting a stronger GSB2 TA signal than the DMF films. Interestingly, GIWAXS and in-situ XRD measurements revealed a similar dependence on the strength of the (002) reflection with solvent (Fig. S3) and with the annealing routine (Fig. 2). Hence, the GSB2 signals observed in chiral perovskite samples appear to be correlated with the presence of (002) oriented in-plane domains, which may promote chiral perovskite/PbI₂ heterostructure formation.

TA kinetics further revealed that GSB1 has a much longer lifetime than GSB2 (Fig. 3h). Inspection of the kinetic traces indicates that the GSB2 feature initially decays quickly (within the first 10 ps), which is consistent with relaxation of states that were directly populated by the photoexcitation. However, the signal recovers after hundreds of picoseconds, corresponding to the timescale on which the GSB1 kinetics change and start to decay more rapidly. Such a behavior points towards excitation transfer from GSB1 to GSB2 after ~100 ps. Time-correlated single-photon counting (TCSPC) measurements were also used to characterize the kinetics of the 510 nm PL feature, which yielded a PL lifetime of ~257 ps (Fig. 3i). No transfer process was detected in the TCSPC measurements, which may be due to its limited time resolution or the transfer process mainly occurring via dark states that can only be detected in TA measurements^{37,38}. However, such a longer PL lifetime (GSB2 lifetime < 100 ps) further suggests the delayed population of the GSB2 transferred from a higher state (GSB1).

Room-temperature excited state polarization dynamics

We further employed circularly polarized TA (CTA) spectroscopy to investigate the polarization dynamics of photoexcited electronic states in our chiral perovskite/PbI₂ thin films at room temperature. We use a linearly polarized pump lasers for photoexcitation, which avoids the generation of polarized populations of excited states due to circularly polarized excitations²¹. Circularly polarized broadband probe pulses were then used to study the intensity of TA signals, and intensities for left-handed and right-handed polarization of probe pulses were compared. Fig. 4a-c show the CTA spectra collected for chiral perovskite/PbI₂ thin films produced using the three different solvents. All three films exhibit intensity differences in the GSB1 regions (~378 nm) for different probe pulse polarizations during the initial 1 ps, which relate to intrinsic chirality features of chiral 1D perovskites (Fig. 3b). The decay kinetics extracted from GSB1 (372-382 nm) are

plotted in Fig. S12. Both DMF and DMSO-DMF films show a long-lived polarization lifetime (a few ns) for chiral 1D perovskite phases, while the polarization in DMSO films only lasts for ~ 1 ps, consistent to the low CD value in these DMSO films (Fig. 3b). Notably, the GSB2 feature, which we attribute to chiral perovskite/PbI₂ heterostructures, shows a non-negligible difference between right-handed (σ^+) and left-handed (σ^-) polarized probes in the DMF-DMSO film (Fig. 4b), indicating successful chirality transfer from the chiral 1D perovskite phase to the PbI₂ phase. No polarization of the GSB2 feature is observed for DMF and DMSO films. We further analyzed the CTA kinetics from the GSB2 regions (490-500 nm) to understand this difference. Since the GSB2 signal is located on a broad photoinduced absorption (PIA) signal extending over the range from 400 to 600 nm, we calculated the pure GSB2 signals by subtracting the adjacent PIA signals (550-560 nm) from the raw signals at the respective GSB2 wavelengths. As shown in the resulting plots of the CTA kinetics in Fig. 4d-f, there is almost no difference between σ^+ and σ^- probes of the GSB2 kinetics for DMF and DMSO films, whereas DMSO-DMF films show a long polarization lifetime reaching ~ 100 ps. Such different polarization characteristics may relate to the solubility of perovskite precursors in different solvents. As widely studied in perovskite film fabrications, DMSO-DMF mixture usually shows better perovskite precursor solubility than pure DMSO or DMF solvent^{39,40}. Thus, PbI₂ nanodomains may be more dispersed in DMSO-DMF films, resulting in faster carrier funnels. More importantly, based on in-situ XRD and GIWAXS results, in-plane (002) facets in DMSO-DMF films may offer a better carrier transport direction between the 1D phase and PbI₂ nanodomains. Therefore, we conclude that chirality transfer of photoexcited electronic states occurs in our chiral 1D perovskites heterostructures which we can control by solvent engineering the film morphology and preferred orientation.

To further study the chirality transfer process in our chiral perovskite heterostructures, we next compared TA data obtained using two different pump wavelengths to excite the chiral perovskite/PbI₂ films. Under 340 nm excitation, both GSB1 at ~ 378 nm and GSB2 at ~ 495 nm are excited, followed by excited state transfer from GSB1 to GSB2, which complicates the relaxation kinetics. However, we can also selectively obtain GSB2 signals under 430 nm excitation. In this case, no broad and long-lived PIA signals appeared together alongside the GSB2 signals, which we can now attribute to transitions from GSB1 to higher-lying states (Fig. S13). Accordingly, there is no carrier transfer between these states under 430 nm excitation⁴¹. As such, a comparison

of differences in the TA kinetics of the GSB2 regions obtained under 340 nm and 430 nm excitation enables the characterization of the carrier transfer process (Fig. 4g-i). For DMF films (Fig. 4g), the decay kinetics from 0.5 ps to 100 ps are almost overlapping for the 340 nm and 430 nm pumps. However, only under 340 nm excitation the TA signal again rises after ~100 ps, which confirms excited state transfer in DMF films after 100 ps. The same trends were also observed in DMSO films (Fig. 4i). In contrast, for the DMF-DMSO films under 340 nm excitation (Fig. 4h), the TA signal exhibits a prominent increase already within 10 ps, compared to TA signals under 430 nm excitation. These results provide a strong indication that charge carrier transfer from GSB1 to GSB2 occurs rapidly in DMF-DMSO films. Based on these observations, we conclude that the strong and long-lived polarization signal in DMF-DMSO films arises from fast carrier transfer, which efficiently delivers polarized excited states from the chiral 1D perovskite phase (GSB1) to the PbI₂ heterostructure (GSB2), before depolarization occurs in the chiral 1D perovskite phase. For DMF and DMSO films, carrier transfer occurs one order of magnitude slower after 100 ps. At this point, the excited state population in the 1D chiral perovskite phase (GSB1) has already depolarized (Fig. S12).

Low-temperature chiroptical features

Given that effective chirality transfer in chiral perovskite/PbI₂ heterostructures enables long-lived polarized states, we attempted to explore the CPL properties of the chiral perovskite/PbI₂ films. However, we did not observe obvious CPL signals due to the low PL intensities from these films at room temperature. Nevertheless, PL features were detected at cryogenic temperatures. Fig. 5a shows the temperature-dependent PL spectra of chiral perovskite DMSO-DMF films. A narrow PL peak at ~498 nm becomes dominant for cryogenic temperatures. This corresponds to a blue shift of the PL emission compared to room temperature (~510 nm). Additionally, the strong increase of intensity, and decrease of peak width, indicate strong electron-phonon interactions in our chiral perovskite/PbI₂ heterostructures. To quantitatively understand electron-phonon coupling in this heterostructure, we extract the integrated intensity of PL peaks from temperature-dependent PL spectra and plot them as a function of temperature (Fig. 5b). In Fig. 5b, the temperature dependence of the integrated PL intensity (I_{PL}) was fitted by the following equation¹²,

$$I_{PL}(T) = \frac{I_0}{1 + A \exp(-E_b/k_B T)} \quad (1)$$

where E_b is the activation energy, here corresponding to the excitonic binding energy, k_B the Boltzmann constant, A a fitting constant, and I_0 the integrated intensity of the PL peak at 5 K. The fitted E_b value is only ~ 11 meV, which is a much smaller value than typically found in low-dimensional perovskite materials (hundreds of meV), and similar to the exciton binding energy reported in PbI_2 ⁴²⁻⁴⁴. Thus, this result is consistent with our conclusion that the sharp PL feature at ~ 500 nm originates from the PbI_2 regions of our chiral perovskite/ PbI_2 heterostructures. Further, these findings explain the low PL intensity of samples at room temperature, since excitons with such a small E_b would have a high probability of thermally dissociating prior to radiatively decaying.

We now compare the PL spectra at 5 K for spin-coated chiral perovskite films prepared with different solvents (Fig. 5c). The PL intensity at ~ 500 nm is much stronger of all chiral perovskite/ PbI_2 films than that of pure PbI_2 films. Additionally, the FWHM of the PL from pure PbI_2 (~ 75 meV) is almost double that of chiral perovskite/ PbI_2 films (~ 38 meV), corroborating our conclusion that the 500 nm PL feature in chiral perovskite films does not simply originate from a pure PbI_2 bulk phase. Furthermore, we hypothesize that the substantial increase in PL intensity of chiral perovskite/ PbI_2 films may be due to carrier funnelling from the perovskite phase to the PbI_2 nanodomains. Consistent with this interpretation, DMSO-DMF films show a much higher PL intensity at ~ 500 nm than pure DMSO or DMF films, as would be expected based on the fast carrier transfer in DMSO-DMF films observed in TA spectroscopy (Fig. 4g-i). This fast process can enable the efficient transfer of carriers to the PbI_2 heterostructure phase before they can recombine via non-radiative decay channels, e.g., at traps and defects.

In the DMF heterostructure films, we find a broad PL feature from 550 nm to 800 nm, which is similar to the PL signals from trapped excitons observed at room temperature (Fig. 1 and 3c). However, at low temperatures, this peak does only appear for DMF heterostructure films. Consistent with our other findings, this result indicates that the use of different solvents during the spin-coating process influences film crystallization, such as higher roughness in DMF films (Fig. S5), leading to the formation of different types and concentrations of traps and defects.

To perform CPL measurements of chiral perovskite films at 5 K, we used linearly polarized pulses to photoexcite the samples, and a quarter waveplate (QWP), followed by a linear polarizer rotated by 45° with respect to the fast axis of the QWP, to select between σ^+ and σ^- PL signals, which were subsequently sent to the camera. Neither chiral perovskite (R) nor (S)-EAPbI₃ DMSO films showed obvious PL intensity differences at ~500 nm between σ^+ and σ^- polarizations (Fig. 5d and 5e). This observation is consistent with their low TA polarization degrees and is a consequence of the slow carrier transfer (Fig. 4g-i). We note that the dominate luminescent species in DMF films are trapped excitons rather than PbI₂ emissions (Fig. 3c and 5c).

For DMSO-DMF films, we find clear intensity differences were detected for chiral (R)- and (S)-EAPbI₃ films between σ^+ and σ^- detections (Fig. 5f and 5g). Using these data, we calculate the degree of CPL polarization (P) by the following equation:

$$P = \frac{I_{\sigma^+} - I_{\sigma^-}}{I_{\sigma^+} + I_{\sigma^-}} \quad (2)$$

Here, I_{σ^+} and I_{σ^-} represent the integrated PL intensities detected for the σ^+ and σ^- polarizations. (R) and (S)-EAPbI₃ films exhibit a similar degree of polarization (~4%) but reversed signs.

To study the excited state polarization dynamics at low temperatures, we additionally performed CTA measurements on chiral perovskite DMSO-DMF films at 5K. In comparison to the room temperature TA signals, the GSB2 signals (495-505 nm) for PbI₂ heterostructures become more pronounced and show longer lifetimes up to a few ns (Fig. S14). Similar to the low-temperature CPL measurements, large polarization in the TA signals for σ^+ and σ^- probes was found at the GSB2 regions (Fig. 5h). The polarization of the GSB2 signal only decays after ~1 ns (Fig. S15), which explains the large degree of CPL at cryogenic temperatures. However, because the GSB2 signals live beyond the end of our temporal detection range and co-exist with time-dependent broad PIA signals, it is difficult to isolate the GSB2 signal at low temperatures and to fit its decay kinetics. Therefore, as an alternative, we choose a PIA region (PIA2, 475-485 nm), which is located next to GSB2, to extract the polarization kinetics. Fig. 5i shows the degree of polarization from the CTA signal (blue line), calculated according to Equation 2, with I_{σ^+} and I_{σ^-} given by the TA intensity obtained for probe pulses with σ^+ and σ^- polarization (red and black lines, respectively). The difference between σ^+ and σ^- probes increases from 1 ps to 4 ps, and stabilizes from 4 ps to

hundreds of ps, reaching a high polarization degree of ~ 0.2 . The rise in polarization kinetics strongly indicates the efficient transfer of chiral excited states from 1D chiral perovskite to a long-lived polarized state in PbI_2 nanodomains. The polarization decreases after ~ 300 ps. Taken together, these results highlight the significant potential of chiral perovskite/ PbI_2 heterostructure films for enabling controllable chirality transfer and circularly polarized emission.

Conclusions

In summary, we demonstrate the synthesis of new low-dimensional chiral perovskite (R/S)- EAPbI_3 single crystals, with single crystal XRD measurements proving that their crystal structures belong to Sohncke space groups. Furthermore, we show that these crystal structures can be transferred to thin film form via dissolution of single crystals in solvents followed by spin coating. In-situ XRD and GIWAXS measurements indicate that the solvents used for the spin-coating process can change the crystal orientations in chiral perovskite films, which enables control of both absorption and CD signals of chiral 1D perovskite films. Transient optical spectroscopy measurements confirm that by simply tuning the solvents used for spin-coating, we can drive fast and effective polarized carrier transfer from chiral perovskite phases to PbI_2 heterostructures, giving rise to a long-lived polarized excited state with circularly polarized emission at low temperatures. Our demonstration of chiral perovskite heterostructures with controllable chirality transfer provides a new avenue for circularly polarized light generation, broadening the material ranges for future non-linear optoelectronics and spintronics applications.

Materials and Methods

Materials

(R)-(+)- α -Ethylbenzylamine, (S)-(-)- α -ethylbenzylamine ((R/S)-EA), lead oxide (PbO), hydroiodic acid (HI , $\geq 47\%$), dimethyl sulfoxide (DMSO, anhydrous) and N,N-dimethylformamide (DMF, anhydrous) were obtained from Sigma-Aldrich and were used directly without further purification.

Fabrication of chiral perovskite single crystals and thin films

The chiral perovskite single crystals were prepared by hydrothermal synthesis. For a general process, 200 mg PbO and 200 μL (R/S)-EA were separately dissolved in 6 mL HI solutions at 95

°C. The resulting solutions were transferred to 25 mL autoclaves and kept at the same temperature (95 °C) inside the oven for 24 h. After slowly decreasing the temperature to room temperature at a rate of 1 °C/h, large needle-shaped single crystals appeared at the bottom of the autoclaves. Diethyl ether was used to clean the obtained crystals three times, after which they were dried under vacuum conditions. The crystals were stored inside a N₂ filled glovebox before usage.

The thin film fabrication process was performed inside a glovebox under inert gas. The stock solution was prepared by mixing single crystal samples (80 mg) in 400 µL pure DMF, DMSO, or 1:1 mixed DMSO-DMF solutions. After fully dissolving the single crystals at 100 °C, 90 µL of the solutions were spin-coated on 20×20 mm pre-cleaned glass substrates (4000 rpm, 35 s). The films were then annealed at 100 °C for 10 min and then stored within a glovebox before characterization.

General structural and optical measurements

In-situ XRD measurements were performed at beamline 12.3.2 at the Advanced Light Source at Lawrence Berkeley National Laboratory utilizing a customized spin-coating setup. For such measurements, the sample was placed at an incident angle of 1° in the X-ray beam and the signal was recorded utilizing a DECTRIS Pilatus 1 M X-ray detector placed at 35° relative to the sample. Images were recorded with an exposure time of 1 s. To avoid oxidation effects during the measurement, the sample chamber was constantly purged with nitrogen. The experiments were conducted at a beam energy of 10 keV, corresponding to a wavelength of 1.2398 Å. However, to allow for an easy comparison with steady-state XRD data, the reflections displayed in this work were re-calculated to match the wavelength of Cu K α 1 radiation.

The GIWAXS measurements were performed at Beamline PO3 at Deutsches Elektronen-Synchrotron (DESY, Hamburg) under an incidence angle of 0.4° with an X-ray beam energy of 11.87 keV. The data were recorded with an exposure time of 1 s on a Lambda 9M detector (X-Spectrum). The reshaped GIWAXS, index, and line cuts of scattering data were performed with the python tool INSIGHT⁴⁵. Single crystal XRD measurements were performed on a Bruker D8 Venture system with Mo radiation ($\lambda = 0.71073$ Å) at 100 K, for further details see the Supporting Information.

AFM measurements were performed in tapping mode with the commercial AFM (Neaspec, Attocube GmbH). The PtIr alloy-coated silicon tips were driven near their resonance frequency of 280 kHz with the free tapping amplitude of ~ 70 nm. Absorption and CD measurements were performed on a commercial CD spectrometer (JASCO J-1700).

PL measurements

Room-temperature PL measurements were conducted using a home-built setup. A Yb:YAG laser system (LightConversion Pharos) with an optical parametric amplifier (LightConversion Orpheus) was used to provide suitable excitation, with wavelengths indicated in the main text. The ICCD camera (Andor, iStar) was used to acquire the PL signals. For low-temperature PL measurements, a Montana cryostation was used to cool down the samples to ~ 5 K. For CPL measurements, an additional quarter waveplate and a linear polarizer were placed in front of the camera to control the detection polarizations. TCSPC measurements were performed using a PicoQuant PDL 800-D excitation laser (405 nm) and a Horiba iHR 550 spectrometer. A constant fraction discriminator (PicoQuant PicoHarp 300) and a single-photon avalanche photodiode detector (Micro Photon Devices PD-100-CTE) were used to collect PL signals.

TA spectroscopy measurements

Room-temperature TA measurements were performed using a commercial TA setup (Ultrafast Systems, HELIOS). An additional linear polarizer and quarter waveplate were placed in front of the samples to change the polarization of the probe beam for CTA measurements. Low-temperature TA measurements were performed using a home-built setup using the same Montana cryostation that was used for PL measurements. Pump and probed beams were generated with a LightConversion Pharos with an optical parametric amplifier (LightConversion, Orpheus) producing 270 fs pulses (5 kHz repetition rate, 780 nm). After splitting this output with a beam splitter, one portion of the beam was directed through a CaF₂ crystal window to generate a white light probe (390 - 780 nm). The other portion of the beam was passed through a linear translation stage (Newport DLS325) and a BBO crystal to provide a 390 nm pump beam. The pump beam was then chopped and overlapped with the probe on the sample. The probe beam was finally collected by an Andor Kymera 193i spectrometer and Andor Zyla 5.5 sCMOS camera. Similar to the room temperature CTA, a linear polarizer and quarter waveplate were used to obtain low-

temperature CTA signals.

References

- (1) Kim, Y.-H.; Zhai, Y.; Lu, H.; Pan, X.; Xiao, C.; Gaubing, E. A.; Harvey, S. P.; Berry, J. J.; Valy Vardeny, Z.; Luther, J. M.; Beard, M. C. Chiral-Induced Spin Selectivity Enables a Room-Temperature Spin Light-Emitting Diode. *Science* **2021**, *371* (6534), 1129–1133.
- (2) Kim, J. S.; Heo, J. M.; Park, G. S.; Woo, S. J.; Cho, C.; Yun, H. J.; Kim, D. H.; Park, J.; Lee, S. C.; Park, S. H.; Yoon, E.; Greenham, N. C.; Lee, T. W. Ultra-Bright, Efficient and Stable Perovskite Light-Emitting Diodes. *Nature* **2022**, *611* (7937), 688–694. <https://doi.org/10.1038/s41586-022-05304-w>.
- (3) Chen, C.; Gao, L.; Gao, W.; Ge, C.; Du, X.; Li, Z.; Yang, Y.; Niu, G.; Tang, J. Circularly Polarized Light Detection Using Chiral Hybrid Perovskite. *Nat Commun* **2019**, *10* (1), 1927. <https://doi.org/10.1038/s41467-019-09942-z>.
- (4) Ishii, A.; Miyasaka, T. Direct Detection of Circular Polarized Light in Helical 1D Perovskite-Based Photodiode. *Sci. Adv* **2020**, *6* (46), eabd3274.
- (5) Yu, D.; Pan, M.; Liu, G.; Jiang, X.; Wen, X.; Li, W.; Chen, S.; Zhou, W.; Wang, H.; Lu, Y.; Ma, M.; Zang, Z.; Cheng, P.; Ji, Q.; Zheng, F.; Ning, Z. Electron-Withdrawing Organic Ligand for High-Efficiency All-Perovskite Tandem Solar Cells. *Nat Energy* **2024**. <https://doi.org/10.1038/s41560-023-01441-2>.
- (6) Qin, C.; Sandanayaka, A. S. D.; Zhao, C.; Matsushima, T.; Zhang, D.; Fujihara, T.; Adachi, C. Stable Room-Temperature Continuous-Wave Lasing in Quasi-2D Perovskite Films. *Nature* **2020**, *585* (7823), 53–57. <https://doi.org/10.1038/s41586-020-2621-1>.
- (7) Ma, J.; Fang, C.; Chen, C.; Jin, L.; Wang, J.; Wang, S.; Tang, J.; Li, D. Chiral 2D Perovskites with a High Degree of Circularly Polarized Photoluminescence. *ACS Nano* **2019**, *13* (3), 3659–3665. <https://doi.org/10.1021/acsnano.9b00302>.
- (8) Di Nuzzo, D.; Cui, L.; Greenfield, J. L.; Zhao, B.; Friend, R. H.; Meskers, S. C. J. Circularly Polarized Photoluminescence from Chiral Perovskite Thin Films at Room Temperature. *ACS Nano* **2020**, *14* (6), 7610–7616. <https://doi.org/10.1021/acsnano.0c03628>.
- (9) Liu, S.; Kepenekian, M.; Bodnar, S.; Feldmann, S.; Heindl, M. W.; Fehn, N.; Zerhoch, J.; Shcherbakov, A.; Pöthig, A.; Li, Y.; Paetzold, U. W.; Kartouzian, A.; Sharp, I. D.; Katan, C.; Even, J.; Deschler, F. Bright Circularly Polarized Photoluminescence in Chiral Layered Hybrid Lead-Halide Perovskites. *Sci. Adv.* **2023**, *9*, eadh5083.
- (10) Yuan, C.; Li, X.; Semin, S.; Feng, Y.; Rasing, T.; Xu, J. Chiral Lead Halide Perovskite Nanowires for Second-Order Nonlinear Optics. *Nano Lett* **2018**, *18* (9), 5411–5417. <https://doi.org/10.1021/acs.nanolett.8b01616>.
- (11) You, Y. M.; Liao, W. Q.; Zhao, D.; Ye, H. Y.; Zhang, Y.; Zhou, Q.; Niu, X.; Wang, J.; Li, P. F.; Fu, D. W.; Wang, Z.; Gao, S.; Yang, K.; Liu, J. M.; Li, J.; Yan, Y.; Xiong, R. G. An Organic-Inorganic Perovskite Ferroelectric with Large Piezoelectric Response. *Science* **2017**, *357* (6348), 306–309. <https://doi.org/10.1126/science.aai8535>.
- (12) Qin, Y.; Gao, F. F.; Qian, S.; Guo, T. M.; Gong, Y. J.; Li, Z. G.; Su, G. D.; Gao, Y.; Li, W.; Jiang, C.; Lu, P.; Bu, X. H. Multifunctional Chiral 2D Lead Halide Perovskites with Circularly Polarized Photoluminescence and Piezoelectric Energy Harvesting Properties. *ACS Nano* **2022**, *16* (2), 3221–3230. <https://doi.org/10.1021/acsnano.1c11101>.
- (13) Wei, Q.; Ning, Z. Chiral Perovskite Spin-Optoelectronics and Spintronics: Toward Judicious Design and Application. *ACS Mater. Lett.* **2021**, *3* (9), 1266–1275. <https://doi.org/10.1021/acsmaterialslett.1c00274>.
- (14) Lu, H.; Wang, J.; Xiao, C.; Pan, X.; Chen, X.; Brunecky, R.; Berry, J. J.; Zhu, K.; Beard, M. C.; Valy Vardeny, Z. Spin-Dependent Charge Transport through 2D Chiral Hybrid Lead-Iodide Perovskites. *Sci. Adv* **2019**, *5* (12), eaay0571.

- (15) Long, G.; Sabatini, R.; Saidaminov, M. I.; Lakhwani, G.; Rasmita, A.; Liu, X.; Sargent, E. H.; Gao, W. Chiral-Perovskite Optoelectronics. *Nat. Rev. Mater.* **2020**, *5* (6), 423–439. <https://doi.org/10.1038/s41578-020-0181-5>.
- (16) Ahn, J.; Lee, E.; Tan, J.; Yang, W.; Kim, B.; Moon, J. A New Class of Chiral Semiconductors: Chiral-Organic-Molecule-Incorporating Organic-Inorganic Hybrid Perovskites. *Mater Horiz* **2017**, *4* (5), 851–856. <https://doi.org/10.1039/c7mh00197e>.
- (17) Ma, J.; Wang, H.; Li, D. Recent Progress of Chiral Perovskites: Materials, Synthesis, and Properties. *Advanced Materials* **2021**, *33*, 2008785. <https://doi.org/10.1002/adma.202008785>.
- (18) Georgieva, Z. N.; Bloom, B. P.; Ghosh, S.; Waldeck, D. H. Imprinting Chirality onto the Electronic States of Colloidal Perovskite Nanoplatelets. *Advanced Materials* **2018**, *30* (23), 1800097. <https://doi.org/10.1002/adma.201800097>.
- (19) Wen, Z.; Lu, R.; Gu, F.; Zheng, K.; Zhang, L.; Jin, H.; Chen, Y.; Wang, S.; Pan, S. Enabling Efficient Blue-Emissive Circularly Polarized Luminescence by in Situ Crafting of Chiral Quasi-2D Perovskite Nanosheets within Polymer Nanofibers. *Adv Funct Mater* **2023**, *33* (7), 2212095. <https://doi.org/10.1002/adfm.202212095>.
- (20) Ye, C.; Jiang, J.; Zou, S.; Mi, W.; Xiao, Y. Core-Shell Three-Dimensional Perovskite Nanocrystals with Chiral-Induced Spin Selectivity for Room-Temperature Spin Light-Emitting Diodes. *J. Am. Chem. Soc.* **2022**, *144* (22), 9707–9714. <https://doi.org/10.1021/jacs.2c01214>.
- (21) Liu, S.; Heindl, M. W.; Fehn, N.; Caicedo-Dávila, S.; Eyre, L.; Kronawitter, S. M.; Zerhoch, J.; Bodnar, S.; Shcherbakov, A.; Stadlbauer, A.; Kieslich, G.; Sharp, I. D.; Egger, D. A.; Kartouzian, A.; Deschler, F. Optically Induced Long-Lived Chirality Memory in the Color-Tunable Chiral Lead-Free Semiconductor (R)/(S)-CHEA4Bi2BrxI10-x (X= 0–10). *J. Am. Chem. Soc.* **2022**, *144* (31), 14079–14089. <https://doi.org/10.1021/jacs.2c01994>.
- (22) Di Nuzzo, D.; Cui, L.; Greenfield, J. L.; Zhao, B.; Friend, R. H.; Meskers, S. C. J. Circularly Polarized Photoluminescence from Chiral Perovskite Thin Films at Room Temperature. *ACS Nano* **2020**, *14* (6), 7610–7616. <https://doi.org/10.1021/acsnano.0c03628>.
- (23) Long, G.; Jiang, C.; Sabatini, R.; Yang, Z.; Wei, M.; Quan, L. N.; Liang, Q.; Rasmita, A.; Askerka, M.; Walters, G.; Gong, X.; Xing, J.; Wen, X.; Quintero-Bermudez, R.; Yuan, H.; Xing, G.; Wang, X. R.; Song, D.; Voznyy, O.; Zhang, M.; Hoogland, S.; Gao, W.; Xiong, Q.; Sargent, E. H. Spin Control in Reduced-Dimensional Chiral Perovskites. *Nat. Photon.* **2018**, *12* (9), 528–533. <https://doi.org/10.1038/s41566-018-0220-6>.
- (24) Hu, Y.; Florio, F.; Chen, Z.; Adam Phelan, W.; Siegler, M. A.; Zhou, Z.; Guo, Y.; Hawks, R.; Jiang, J.; Feng, J.; Zhang, L.; Wang, B.; Wang, Y.; Gall, D.; Palermo, E. F.; Lu, Z.; Sun, X.; Lu, T.-M.; Zhou, H.; Ren, Y.; Wertz, E.; Sundararaman, R.; Shi, J. A Chiral Switchable Photovoltaic Ferroelectric 1D Perovskite. *Sci. Adv* **2020**, *6*, eaay4213.
- (25) Jana, M. K.; Song, R.; Xie, Y.; Zhao, R.; Sercel, P. C.; Blum, V.; Mitzi, D. B. Structural Descriptor for Enhanced Spin-Splitting in 2D Hybrid Perovskites. *Nat. Commun.* **2021**, *12* (1), 4982. <https://doi.org/10.1038/s41467-021-25149-7>.
- (26) Smith, M. D.; Karunadasa, H. I. White-Light Emission from Layered Halide Perovskites. *Acc Chem Res* **2018**, *51* (3), 619–627. <https://doi.org/10.1021/acs.accounts.7b00433>.
- (27) Yuan, Z.; Zhou, C.; Tian, Y.; Shu, Y.; Messier, J.; Wang, J. C.; Van De Burgt, L. J.; Kountouriotis, K.; Xin, Y.; Holt, E.; Schanze, K.; Clark, R.; Siegrist, T.; Ma, B. One-Dimensional Organic Lead Halide Perovskites with Efficient Bluish White-Light Emission. *Nat. Commun.* **2017**, *8*. <https://doi.org/10.1038/ncomms14051>.
- (28) Urban, J. M.; Jouaiti, A.; Gruber, N.; Delpont, G.; Trippé-Allard, G.; Guillemoles, J. F.; Deleporte, E.; Ferlay, S.; Garrot, D. Using Chiral Ammonium Cations to Modulate the Structure of 1D Hybrid Lead Bromide Perovskites for Linearly Polarized Broadband Light Emission at Room Temperature. *J Mater Chem C* **2022**, *10* (34), 12436–12443. <https://doi.org/10.1039/d2tc02040h>.

- (29) Zhu, H.; Wang, Q.; Sun, K.; Chen, W.; Tang, J.; Hao, J.; Wang, Z.; Sun, J.; Choy, W. C. H.; Müller-Buschbaum, P.; Sun, X. W.; Wu, D.; Wang, K. Solvent Modulation of Chiral Perovskite Films Enables High Circularly Polarized Luminescence Performance from Chiral Perovskite/Quantum Dot Composites. *ACS Appl. Mater. Interfaces* **2023**, *15*, 9978–9986. <https://doi.org/10.1021/acsmi.2c20716>.
- (30) Zanetta, A.; Larini, V.; Vikram; Toniolo, F.; Vishal, B.; Elmetekawy, K. A.; Du, J.; Scardina, A.; Faini, F.; Pica, G.; Pirota, V.; Pitaro, M.; Marras, S.; Ding, C.; Yildirim, B. K.; Babics, M.; Ugur, E.; Aydin, E.; Ma, C. Q.; Doria, F.; Loi, M. A.; De Bastiani, M.; Herz, L. M.; Portale, G.; De Wolf, S.; Islam, M. S.; Grancini, G. Vertically Oriented Low-Dimensional Perovskites for High-Efficiency Wide Band Gap Perovskite Solar Cells. *Nat Commun* **2024**, *15* (1), 9069. <https://doi.org/10.1038/s41467-024-53339-6>.
- (31) Nina Berova; Koji Nakanishi; Robert W. Woody. *Circular Dichroism: Principles And*, John Wiley & Sons.; 2000.
- (32) Heindl, M. W.; Kodalle, T.; Fehn, N.; Reb, L. K.; Liu, S.; Harder, C.; Abdelsamie, M.; Eyre, L.; Sharp, I. D.; Roth, S. V.; Müller-Buschbaum, P.; Kartouzian, A.; Sutter-Fella, C. M.; Deschler, F. Strong Induced Circular Dichroism in a Hybrid Lead-Halide Semiconductor Using Chiral Amino Acids for Crystallite Surface Functionalization. *Adv. Opt. Mater.* **2022**, *10* (14), 2200204. <https://doi.org/10.1002/adom.202200204>.
- (33) Liu, J.; Sun, Y.; Zhou, Y.; Zhang, C.; Wang, X.; Wang, L.; Xiao, M. Few-Layer PbI₂ Nanoparticle: A 2D Semiconductor with Lateral Quantum Confinement. *Journal of Physical Chemistry Letters* **2019**, *10* (24), 7863–7869. <https://doi.org/10.1021/acs.jpcclett.9b03009>.
- (34) Zhang, D.; Liu, Y.; He, M.; Zhang, A.; Chen, S.; Tong, Q.; Huang, L.; Zhou, Z.; Zheng, W.; Chen, M.; Braun, K.; Meixner, A. J.; Wang, X.; Pan, A. Room Temperature near Unity Spin Polarization in 2D Van Der Waals Heterostructures. *Nat Commun* **2020**, *11*, 4442. <https://doi.org/10.1038/s41467-020-18307-w>.
- (35) Ismail, R. A.; Mousa, A. M.; Khashan, K. S.; Mohsin, M. H.; Hamid, M. K. Synthesis of PbI₂ Nanoparticles by Laser Ablation in Methanol. *J. Mater. Sci.: Mater. Electron.* **2016**, *27* (10), 10696–10700. <https://doi.org/10.1007/s10854-016-5169-y>.
- (36) Gull, S.; Jamil, M. H.; Zhang, X.; Kwok, H. sing; Li, G. Stokes Shift in Inorganic Lead Halide Perovskites: Current Status and Perspective. *ChemistryOpen* **2022**, *11* (3), e2021002. <https://doi.org/10.1002/open.202100285>.
- (37) Feldmann, S.; Macpherson, S.; Senanayak, S. P.; Abdi-Jalebi, M.; Rivett, J. P. H.; Nan, G.; Tainter, G. D.; Doherty, T. A. S.; Frohna, K.; Ringe, E.; Friend, R. H.; Sirringhaus, H.; Saliba, M.; Beljonne, D.; Stranks, S. D.; Deschler, F. Photodoping through Local Charge Carrier Accumulation in Alloyed Hybrid Perovskites for Highly Efficient Luminescence. *Nat Photonics* **2020**, *14* (2), 123–128. <https://doi.org/10.1038/s41566-019-0546-8>.
- (38) Hoye, R. L. Z.; Eyre, L.; Wei, F.; Brivio, F.; Sadhanala, A.; Sun, S.; Li, W.; Zhang, K. H. L.; MacManus-Driscoll, J. L.; Bristowe, P. D.; Friend, R. H.; Cheetham, A. K.; Deschler, F. Fundamental Carrier Lifetime Exceeding 1 μ s in Cs₂AgBiBr₆ Double Perovskite. *Adv. Mater. Interfaces* **2018**, *5* (15), 1800464. <https://doi.org/10.1002/admi.201800464>.
- (39) Petrov, A. A.; Ordinartsev, A. A.; Fateev, S. A.; Goodilin, E. A.; Tarasov, A. B. Solubility of Hybrid Halide Perovskites in Dmf and DmsO. *Molecules* **2021**, *26* (24), 7541. <https://doi.org/10.3390/molecules26247541>.
- (40) Huang, P. H.; Wang, Y. H.; Ke, J. C.; Huang, C. J. The Effect of Solvents on the Performance of CH₃NH₃PbI₃ Perovskite Solar Cells. *Energies* **2017**, *10* (5). <https://doi.org/10.3390/en10050599>.
- (41) Zhang, J.; Zhu, X.; Wang, M.; Hu, B. Establishing Charge-Transfer Excitons in 2D Perovskite Heterostructures. *Nat. Commun.* **2020**, *11* (1), 2618. <https://doi.org/10.1038/s41467-020-16415-1>.

- (42) Chen, X.; Lu, H.; Wang, K.; Zhai, Y.; Lunin, V.; Sercel, P. C.; Beard, M. C. Tuning Spin-Polarized Lifetime in Two-Dimensional Metal-Halide Perovskite through Exciton Binding Energy. *J. Am. Chem. Soc.* **2021**, *143* (46), 19438–19445. <https://doi.org/10.1021/jacs.1c08514>.
- (43) Valastro, S.; Gavranovic, S.; Deretzis, I.; Vala, M.; Smecca, E.; La Magna, A.; Alberti, A.; Castkova, K.; Mannino, G. Temperature-Dependent Excitonic Band Gap in Lead-Free Bismuth Halide Low-Dimensional Perovskite Single Crystals. *Adv Opt Mater* **2023**. <https://doi.org/10.1002/adom.202302397>.
- (44) J. Bordas; E.A. Davis. The Excitons at the Band Edge of Pbl₂. *Solid State Commun* **1973**, *12* (7), 717–720.
- (45) Reus, M. A.; Reb, L. K.; Weinzierl, A. F.; Weindl, C. L.; Guo, R.; Xiao, T.; Schwartzkopf, M.; Chumakov, A.; Roth, S. V.; Müller-Buschbaum, P. Time-Resolved Orientation and Phase Analysis of Lead Halide Perovskite Film Annealing Probed by in Situ GIWAXS. *Adv Opt Mater* **2022**, *10* (14), 2102722. <https://doi.org/10.1002/adom.202102722>.

Acknowledgements

This research used resources of the Advanced Light Source, which is a DOE Office of Science User Facility under contract no. DE-AC02-05CH11231. Specifically, Beamline 12.3.2 was used. The authors would further like to thank Dr. Nobumichi Tamura for his on-site support at the ALS and for the provision of data processing software. Work at the Molecular Foundry was supported by the Office of Science, Office of Basic Energy Sciences, of the U.S. Department of Energy under Contract No. DE-AC02-05CH11231. We thank Dr. Matthias Schwarzkopf for the help at Beamline PO3, Desy. The static GIWAXS measurement was done at the light source PETRA III AT DESY, a member of the Helmholtz Association (HGF).

Funding

This project has received funding from the European Research Council (ERC Starting Grant agreement no. 852084 — TWIST). F. D acknowledges the financial support from the Deutsche Forschungsgemeinschaft (DFG) under Emmy Noether Program (Project 387651688). This work received support from the Deutsche Forschungsgemeinschaft (DFG, German Research Foundation) under Germany's Excellence Strategy – EXC 2089/1 – 390776260, as well as from TUM.solar in the context of the Bavarian Collaborative Research Project Solar Technologies Go Hybrid (SolTech). P.M.-B. thanks Deutsche Forschungsgemeinschaft (DFG) for financial support via the International Research Training Group 2022 the Alberta/Technical University of Munich International Graduate School for Environmentally Responsible Functional Materials (ATUMS) and under Germany's Excellence Strategy – EXC 2089/1 – 390776260 (e-conversion) as well as from TUM.solar in the context of the Bavarian Collaborative Research Project Solar Technologies

Go Hybrid (SolTech). S.L. and K.S. acknowledge the financial support from the China Scholarship Council (CSC).

Author contributions

S.L. and F.D. conceived the ideas and designed the experiments for this project. F.D., U.W.P., I.D.S, and P. M.-B. supervised the project. S.L. and C.Z. performed single crystal and thin film fabrication. S.L. and C.Z. conducted absorption, CD, PL, TRPL, TA, and CTA measurements. S.L., S.B., M.M. and J.Z. performed CPL measurements. J.Z. and M.W.H performed in-situ XRD measurements with the help from T.K. and C.M.S.-F. C.J., J.B., and A.P. carried out SCXRD measurements and analysis. A.S. conducted AFM measurements. S.L. drafted the manuscript with a discussion of results, revisions, and comments on the manuscript from all authors.

Competing interests: Authors declare that they have no competing interests.

Data and materials availability: All data are available in the main text or the supplementary materials.

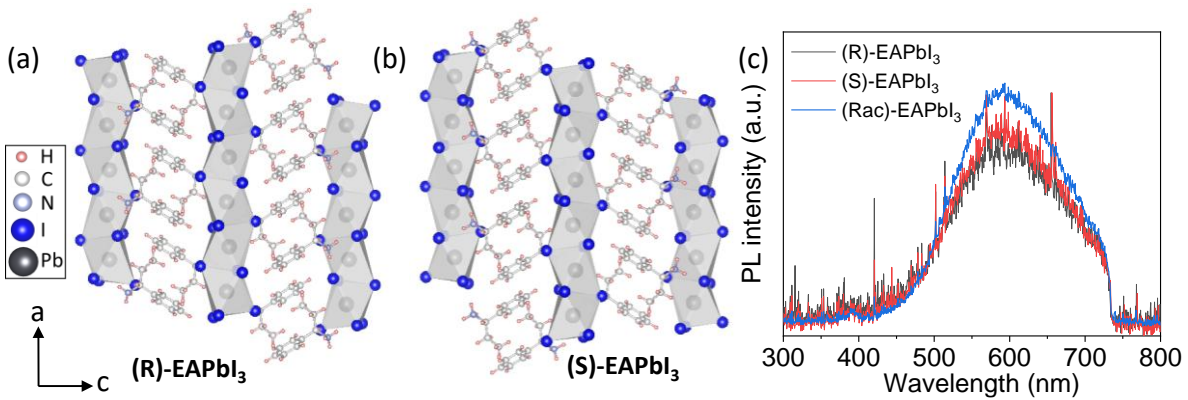


Fig. 1. Structural and emission characterization of chiral 1D (R/S/Rac)-EAPbI₃ perovskite single crystals. (a, b) Structure of (R/S)-EAPbI₃ from single-crystal X-ray diffraction. (c) Room-temperature PL spectra collected from chiral (R/S/Rac)-EAPbI₃ single crystals, respectively.

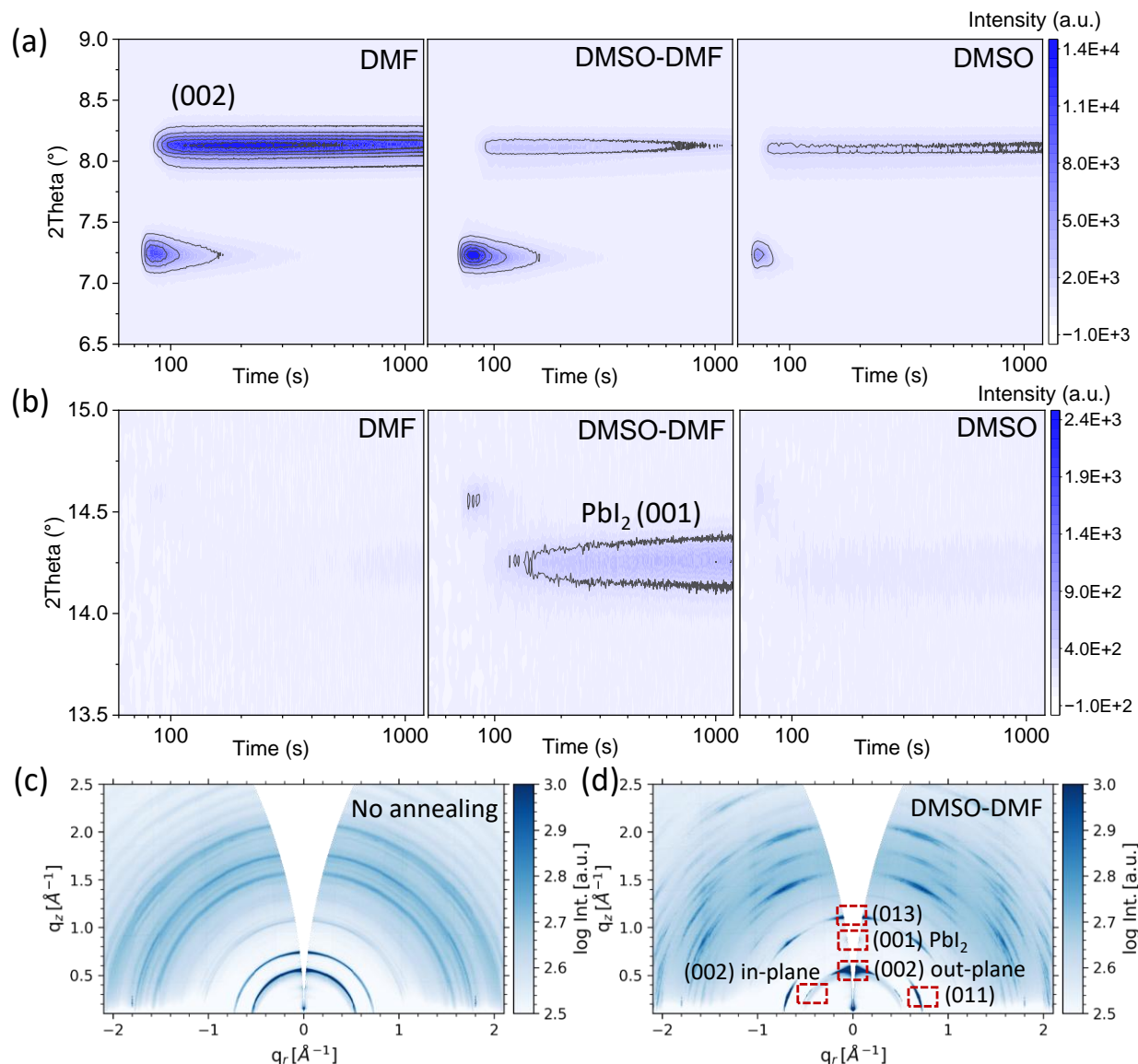


Fig. 2. Structural evolution of chiral 1D (R)-EAPbI₃/PbI₂ thin films during spin-coating. (a, b) In-situ XRD maps of chiral perovskite/PbI₂ thin films monitored during spin-coating (before 60 s) and during the subsequent annealing process at 100 °C (after 60 s). The films were fabricated using three different solvents, DMF, DMSO, and a 1:1 DMF-DMSO mixture. The XRD patterns are expanded in two different regions, 6.5 to 9.0° (a), and 13.5 to 15.0° (b). (c, d) 2D GIWAXS data for perovskite films fabricated using a 1:1 DMSO-DMF mixture (c) without and (d) with a 10 min annealing process at 100 °C.

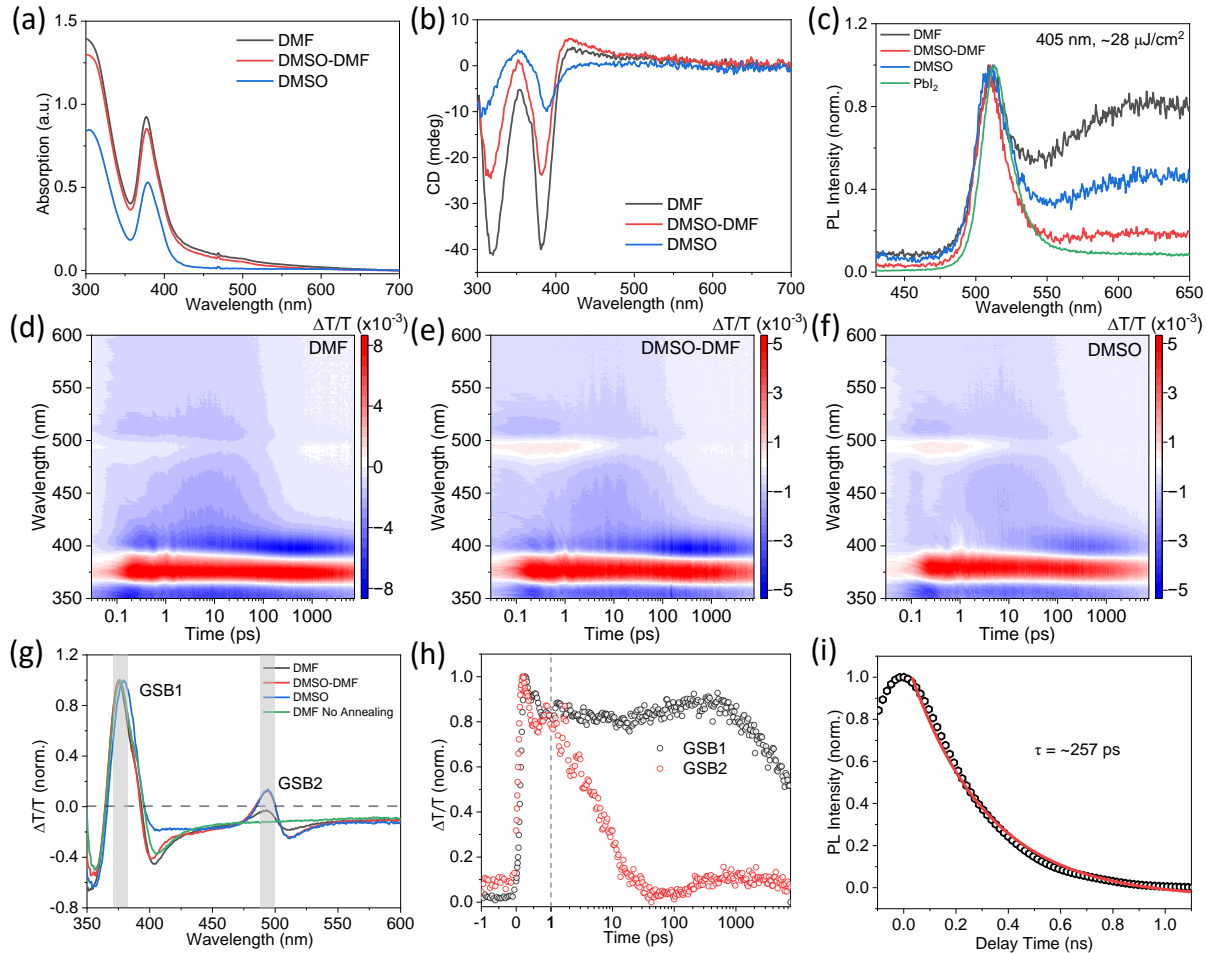


Fig. 3. Photophysics and excited state dynamics in chiral (R)-EAPbI₃/PbI₂ thin films. (a) Steady-state room-temperature UV-vis absorption, (b) circular dichroism, and (c) PL spectra of chiral perovskite thin films. (d-f) Transient absorption (pump wavelength 340 nm, fluence $\sim 180 \mu\text{J}/\text{cm}^2$) color maps of chiral perovskite thin films formed using DMF (d), mixed DMSO-DMF (e), and DMSO solvents (f). (g) Comparison of TA spectra averaged over the initial 1 ps after excitation of films prepared from different solvents. The thin films were annealed at 100°C for 10 min. One DMF-derived film was fabricated without annealing for comparison. Grey regions indicate regions of two GSB signals. (h) TA kinetics extracted from the two GSB regions highlighted in (g) of the annealed DMF-derived film. The GSB2 kinetics were corrected for the underlying broad photoinduced absorption by subtracting the signal in the range 550-560 nm. (i) TCSPC kinetics of the annealed DMF-derived film, obtained at a luminescence detection wavelength of 505 nm (excitation wavelength 405 nm, fluence of $\sim 10 \mu\text{J}/\text{cm}^2$).

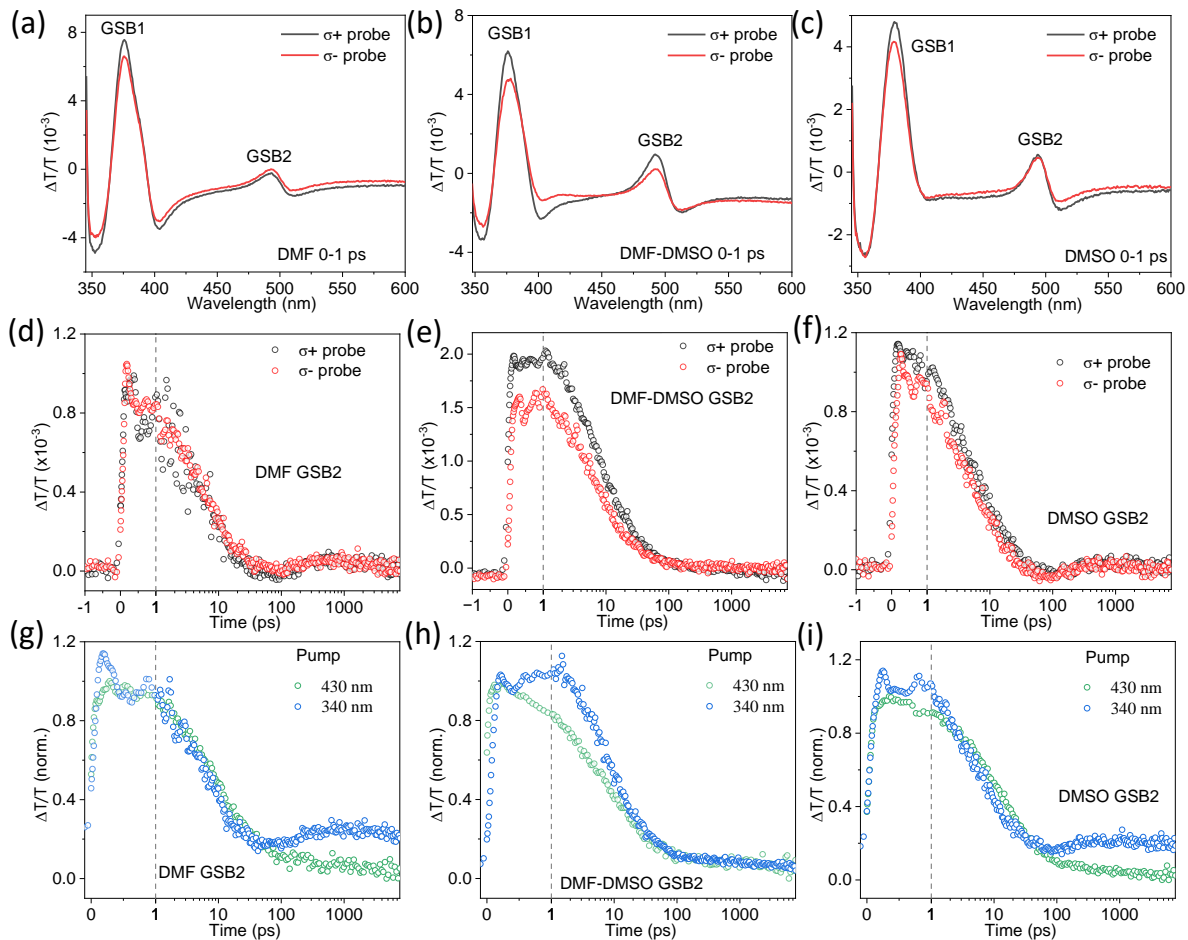


Fig. 4. Photoexcited state polarization dynamics in chiral (R)-EAPbI₃/PbI₂ thin films. (a-c) CTA spectra in the initial 1 ps after excitation for chiral perovskite thin films deposited using (a) DMF, (b) DMF-DMSO, and (c) DMSO. A linearly polarized 340 nm ($\sim 180 \mu\text{J}/\text{cm}^2$) pump was used to excite each of the samples. Circularly polarized right-handed (σ^+) and left-handed (σ^-) probes were used to detect TA signals. (d-f) CTA kinetics collected from GSB2 regions from panels in Fig. 4a-c, respectively. (g-f) Comparison of linear TA kinetics at GSB2 regions under 340 nm and 430 nm excitations. The TA kinetics were obtained from (g) DMF, (h) DMSO-DMF, and (i) DMSO films.

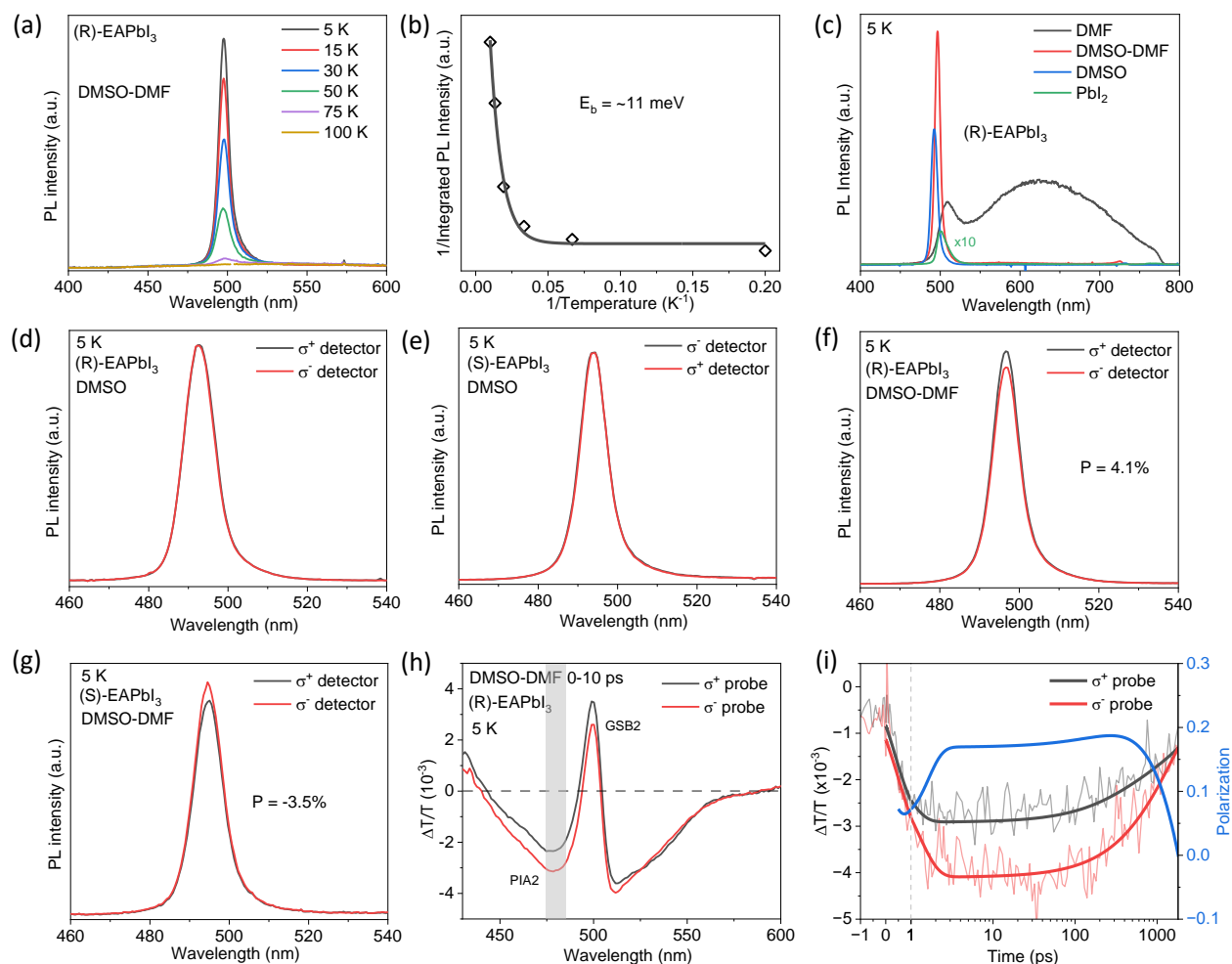


Fig. 5. Chiroptical photophysics of chiral perovskite/PbI₂ thin films at cryogenic temperatures. (a, b) Temperature-dependent PL spectra (a), and corresponding integrated PL intensity (b) as a function of temperature for chiral perovskite films deposited with DMSO-DMF. The samples were excited at 395 nm with a pump fluence of $\sim 5 \mu\text{J}/\text{cm}^2$. (c) Comparison of low temperature (5 K) PL spectra of films deposited using DMF, mixed DMSO-DMF, and DMSO solutions. (d-g) Low-temperature (5 K) CPL spectra of chiral perovskite/PbI₂ films produced using (d, e) DMSO, and (f, g) mixed DMSO-DMF. (h, i) Low temperature (5 K) CTA spectra (h) and kinetics (i) of chiral perovskite films produced using DMSO-DMF. The CTA kinetics were collected from the PIA signals, as indicated by the grey region in (h). The samples were excited at 390 nm with a pump fluence of $\sim 14 \mu\text{J}/\text{cm}^2$.